

Preclinical evaluation of [^{111}In]MICA-401, an activity-based probe for SPECT imaging of *in vivo* uPA activity

Christel Vangestel^{a,b}, David Thomae^{a,c}, Jeroen Van Soom^c, Johan Ides^d, Leonie wyffels^{a,b}, Patrick Pauwels^{d,e}, Sigrid Stroobants^{a,b}, Pieter Van der Veken^c, Viktor Magdolen^f, Jurgen Joossens^c, Koen Augustyns^c and Steven Staelens^{a*}



Urokinase-type plasminogen activator (uPA) and its inhibitor PAI-1 are key players in cancer invasion and metastasis. Both uPA and PAI-1 have been described as prognostic biomarkers; however, non-invasive methods measuring uPA activity are lacking. We developed an indium-111 (^{111}In)-labelled activity-based probe to image uPA activity *in vivo* by single photon emission computed tomography (SPECT). A DOTA-conjugated uPA inhibitor was synthesized and radiolabelled with ^{111}In ([^{111}In]MICA-401), together with its inactive, hydrolysed form ([^{111}In]MICA-402). A biodistribution study was performed in mice (healthy and tumour-bearing), and tumour-targeting properties were evaluated in two different cancer xenografts (MDA-MB-231 and HT29) with respectively high and low levels of uPA expression *in vitro*, with either the active or hydrolysed radiotracer. MicroSPECT was performed 95 h post injection followed by *ex vivo* biodistribution. Tumour uptake was correlated with human and murine uPA expression determined by ELISA and immunohistochemistry (IHC). Biodistribution data with the hydrolysed probe [^{111}In]MICA-402 showed almost complete clearance 95 h post injection. The *ex vivo* biodistribution and SPECT data with [^{111}In]MICA-401 demonstrated similar tumour uptakes in the two models: *ex vivo* $5.68 \pm 1.41\%$ ID/g versus $5.43 \pm 1.29\%$ ID/g and *in vivo* 4.33 ± 0.80 versus 4.86 ± 1.18 for MDA-MB-231 and HT-29 respectively. Human uPA ELISA and IHC showed significantly higher uPA expression in the MDA-MB-231 tumours, while mouse uPA staining revealed similar staining intensities of the two tumours. Our data demonstrate non-invasive imaging of uPA activity *in vivo*, although the moderate tumour uptake and hence potential clinical translation of the radiotracer warrants further investigation. Copyright © 2016 John Wiley & Sons, Ltd. Additional supporting information may be found in the online version of this article at the publisher's web site.

Keywords: urokinase-type plasminogen activator; single photon emission computed; tomography; uPA activity; cancer xenografts

1. INTRODUCTION

Enzymatic degradation of the extracellular matrix (ECM) plays an important role in cancer invasion and metastasis. The urokinase-type plasminogen activator (uPA) and its inhibitor PAI-1 are key players in a proteolytic cascade, involved in physiological and pathophysiological degradation and remodelling of the ECM. These processes promote tumour progression, invasion and

metastasis (1,2). uPA is a serine protease, which after binding with the urokinase-type plasminogen activator receptor (uPAR) initiates the conversion of the inactive zymogen plasminogen to plasmin. The protease plasmin triggers fibrinolysis, cleaves a range of ECM components and by activation of matrix metalloproteinase (MMPs) facilitates the degradation of the ECM. Plasmin will also indirectly facilitate release of growth factors from the interstitial matrix and basement membrane (3). uPA is expressed by a variety of cells (including tumour cells) as a proenzyme (pro-uPA), which is converted to its active form by proteolysis. Interestingly this conversion is catalysed by plasmin, thus

* Correspondence to: Steven Staelens, Molecular Imaging Center Antwerp, University of Antwerp, Universiteitsplein 1, B-2610 Antwerp, Belgium. E-mail: steven.staelens@uantwerpen.be

a C. Vangestel, D. Thomae, L. wyffels, S. Stroobants, S. Staelens
Molecular Imaging Center Antwerp, University of Antwerp, Universiteitsplein 1, B-2610 Antwerp, Belgium

b C. Vangestel, L. wyffels, S. Stroobants
Department of Nuclear Medicine, Antwerp University Hospital, Wilrijkstraat 10, B-2650 Edegem, Belgium

c D. Thomae, J. Van Soom, P. Van der Veken, J. Joossens, K. Augustyns
Department of Medicinal Chemistry, University of Antwerp, Universiteitsplein 1, B-2610 Antwerp, Belgium

d J. Ides, P. Pauwels
Center for Oncological Research, University of Antwerp, Universiteitsplein 1, B-2610 Antwerp Belgium

e P. Pauwels
Department of Pathology, Antwerp University Hospital, Wilrijkstraat 10, B-2650 Edegem, Belgium

f V. Magdolen
Klinische Forschergruppe der Frauenklinik, Klinikum rechts der Isar der TU München, 81675 Munich, Germany

creating a positive feedback loop (4,5). The activation of pro-uPA is significantly accelerated upon binding of the pro-enzyme to its specific cell surface receptor (6). Numerous studies examining the uPA system indicate that high levels of uPA and/or PAI-1 in tumours are correlated with poor prognosis. Moreover, these have been validated at the highest level of evidence as clinical biomarkers of prognosis in breast cancer (7–10). Moreover, uPA is also suggested as a prognostic biomarker in other tumour types including lung, prostate, ovarian, cervical, pancreatic, colorectal and gastric cancer (11–17). Determination of uPA and PAI-1 levels is currently done using standardized enzyme-linked immunosorbent assays (ELISAs), thus fresh tissue samples are needed. More importantly, this method lacks the ability to discriminate between active and inactive uPA (pro-uPA) (18). Therefore, the development of non-invasive imaging methods to visualize and quantify uPA activity *in vivo* could be a valuable tool in clinical practice towards patient stratification and therapy monitoring (19–22). In particular, molecular imaging techniques in nuclear medicine serve as highly sensitive tools, which are ideally suited for non-invasive imaging of cancer and small micrometastatic lesions. Targeting uPA with positron emission tomography (PET) or single photon emission computed tomography (SPECT) activity-based imaging probes would hence offer the ability to monitor uPA activity *in vivo*. So far, non-invasive imaging of the uPA system has been limited to imaging probes targeting the uPAR, which may not be an accurate indication of the actual uPA activity in the tumour (23–25), as binding of uPA/pro-uPA to its receptor and activation of pro-uPA are critical steps for cancer cell dissemination (26). A first-in-human clinical trial with PET imaging of uPAR in patients with breast, prostate and bladder cancer has recently been published; high uptake in both primary tumour lesions and lymph node metastases was seen and paralleled high uPAR expression in excised tumour tissue (27).

Previously, our research group reported the synthesis and *in vivo* evaluation of an activity-based [^{18}F]-labelled uPA probe (28). This probe, [^{18}F]**1**, was designed based on a phosphonate scaffold (which binds covalently to uPA) bearing a guanidine group to enhance the selectivity for uPA (29) and a PEG linker to connect to the [^{18}F]-4-fluorobenzoyl group (Fig. 1). However, the aforementioned radiotracer displayed low absolute tumour uptake values due to unfavourable stability and pharmacokinetic properties. The same uPA activity-based probe has now been linked to a DOTA chelator, which is used as a complexing agent for radioisotope indium-111 (^{111}In) (MICA-401, Fig. 1). The affinity and covalent bond formation of MICA-401 for uPA and the selectivity over a set of related trypsin-like serine proteases was analysed.

Finally, the functional activity-based probe [^{111}In]MICA-401 was evaluated for its capacity to image uPA activity *in vivo* by SPECT in two different cancer models, with a confirmed distinct uPA expression *in vitro*. As a control, a corresponding hydrolysed inactive probe ([^{111}In]MICA-402, Fig. 1) was used *in vivo* in both cancer models. This probe serves as a negative control, since we confirmed that MICA-402 has no affinity for uPA and is not able to form a covalent bond with uPA or related proteases.

2. EXPERIMENTAL SECTION

2.1. Organic synthesis

A detailed description of the organic synthesis of compounds MICA-401 and MICA-402 and their corresponding precursor (compounds **3** and **5**, respectively) is provided in the supplementary data.

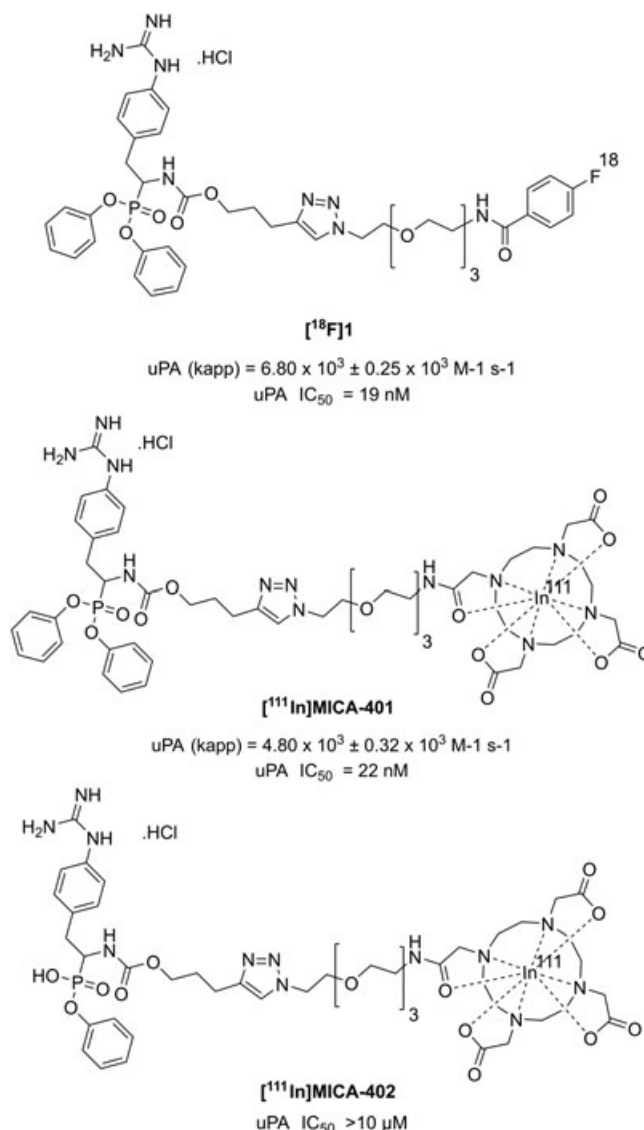


Figure 1. Chemical structures of fluor-18 and indium-111 labelled uPA inhibitors [^{18}F]**1**, [^{111}In]MICA-401 and the uPA hydrolysed probe [^{111}In]MICA-402.

2.2. *In vitro* evaluation of binding kinetics

Previously described methods (29–31) were used to determine the IC_{50} and k_{app} values of compounds uPA-PET, MICA-401 and MICA-402 for uPA, tPA, thrombin, plasmin, FXa, plasma KLK, KLK1, KLK4, KLK8, HNE and acetylcholinesterase (AChE). For HNE we used the same method as described for uPA but with neutrophil elastase (100 μg (Enzo) dissolved in 200 μl 50 mM NaAc, 150 mM NaCl, pH 5.5) as the enzyme solution, MeOSuc-Ala-Ala-Pro-Val-pNA (Enzo, K_m 125 μM) as substrate and a Tris buffer at pH 7.8.

2.3. Radiochemistry

2.3.1. Radiosynthesis of [^{111}In]MICA-401

0.5 M ammonium acetate buffer (pH 5.5, 450 μl) was added to $342.62 \pm 2.22 \text{ MBq}$ [^{111}In]InCl₃ (Mallinckrodt, Petten, The Netherlands). Thirty microlitres of a solution of compound **3** (supplementary data; 1 mg/mL in MeOH) were added and the

solution was heated for 45 min at 60 °C. The reaction mixture was diluted with 200 µL of water and injected into the HPLC loop. The crude reaction mixture was purified on a Chromolith® Performance RP-18e, 5 µm, 100 mm × 4.6 mm eluted with a solution of 0.05 M NaOAc, pH 5.5/EtOH (75/25, v/v) at 1 mL/min. [¹¹¹In]MICA-401 has a retention time of 21–22 min and was collected and the solution was evaporated at 40 °C under a mild flow of compressed air. The volume was adjusted to 1 mL with EtOH and the solution was filtered through a 0.22 µm sterile filter (Pall Acrodisc syringe filter, 13 mm, 0.2 µm) and diluted with 0.9% sodium chloride solution to reach a concentration of EtOH below 10%. [¹¹¹In]MICA-401 was synthesized in a 59% (*n* = 4) yield. Chemical and radiochemical purities (>98%) of the tracer were measured using analytical HPLC (Chromolith® Performance RP-18e, 5 µm, 100 mm × 4.6 mm) eluted with 0.1% TFA in H₂O/0.1% TFA in CH₃CN (78/22, v/v) at flow rate of 1 mL/min. The specific activity was determined using a UV calibration curve (λ = 204 nm) and was in the range of 6–12 GBq/µmol.

2.3.2. Radiosynthesis of [¹¹¹In]MICA-402

0.5 M ammonium acetate buffer (pH 5.5, 450 µL) was added to 354.46 ± 15.54 MBq [¹¹¹In]InCl₃ (Mallinckrodt). Thirty microlitres of a solution of compound **5** (supplementary data; 1 mg/mL in MeOH) was added and the solution was heated for 45 min at 60 °C. The reaction mixture was diluted with 200 µL of water and injected into the HPLC loop. The crude reaction mixture was purified on a Chromolith® Performance RP-18e, 5 µm, 100 mm × 4.6 mm eluted with a solution of 0.05 M NaOAc, pH 5.5/EtOH (90.5/9.5, v/v) at 1 mL/min. [¹¹¹In]MICA-402 has a retention time of 15–16 min and was collected and filtered through a 0.22 µm sterile filter (Pall Acrodisc syringe filter, 13 mm, 0.2 µm). [¹¹¹In]MICA-402 was obtained in a radiochemical yield of 71% (*n* = 2). Chemical and radiochemical purities (>98%) of the tracer were measured using analytical HPLC (Chromolith® Performance RP-18e, 5 µm, 100 mm × 4.6 mm) eluting with 0.1% TFA in H₂O/0.1% TFA in CH₃CN (90/10, v/v) at flow rate of 1 mL/min. The specific activity was determined using a UV calibration curve (λ = 207 nm) and was in the range of 8–10 GBq/µmol.

For the measurement of the partition coefficient, *n*-octanol (1 mL) and 0.01 M phosphate buffered saline (PBS) (pH = 7.4) were added to a test tube and allowed to equilibrate for 10 min. Five microlitres of [¹¹¹In]MICA-401 or [¹¹¹In]MICA-402 was added and vortexed for 2 min at RT. The tube was centrifuged at 3000 rpm for 10 min. Fractions of 500 µL of both phases were put in pre-weighed tubes and measured in the gamma counter. The partition coefficient *D* was calculated as radioactivity (cpm/mL) in *n*-octanol/radioactivity (cpm/mL) in PBS. The log *D* (*n*-octanol/PBS, pH = 7.4) value is given as an average of three measurements. The partition coefficients of [¹¹¹In]MICA-401 and [¹¹¹In]MICA-402 were measured and log *D* values of −2.73 ± 0.01 and −4.15 ± 0.02 were respectively obtained.

2.4. Cell cultures and animal model

Female 6-week-old CD1^{−/−} Foxn1^{nu} mice (*n* = 37) were obtained (25.6 ± 2.1 g) from Charles River Laboratories (L'Arbresle, France). The animals were kept under environmentally controlled conditions (12 h light–dark cycle, 20–24 °C and 40–70% relative humidity) in individually ventilated cages with food and water ad libitum. The study protocol was approved by the local Animal

Experimental Ethical Committee of the University of Antwerp, Belgium (2011–20). All animal studies were ethically reviewed and carried out in accordance with European Directive 86/609/EEC Welfare and Treatment of Animals.

Bioware® MDA-MB-231-luc2-GFP (human breast cancer cell line, Perkin Elmer, Waltham, MA, USA) and HT-29 (human colon adenocarcinoma, ATCC, Rockville, MD, USA) were selected for their different uPA expressions. Secreted uPA has been demonstrated in the culture medium of MDA-MB-231, but not in HT-29 (32,33). Cells were routinely cultured in Dulbecco's modified Eagle medium supplemented with 10% heat-inactivated foetal bovine serum (FBS), 2 mM glutamine, 1% sodium pyruvate and 1% penicillin/streptomycin (Invitrogen, Merelbeke, Belgium). To establish an orthotopic MDA-MB-231 model, approximately 5 × 10⁶ viable MDA-MB-231 cells were resuspended in 100 µL PBS containing Matrigel (1:2 in PBS; BD Bioscience, San Jose, CA, USA) and were subsequently injected in the second left abdominal mammary fat pad. For the HT-29 subcutaneous model, approximately 10 × 10⁶ viable cells, suspended in 100 µL PBS, were inoculated in the right hind leg of the mice. Tumour growth was monitored twice a week with digital calliper measurements starting on detection of palpable tumours. Tumour volume was calculated using the modified ellipsoid formula $\frac{1}{2}(\text{length} \times \text{width}^2)$. Four to six weeks after MDA-MB-231 tumour inoculation, when tumours reached a volume of 150 mm³, and 2–3 weeks after HT-29 tumour inoculation, when tumours reached a volume of 400–500 mm³, mice were subjected to µSPECT/CT imaging.

2.5. Selection of imaging window

To obtain the optimal time point for µSPECT imaging, a biodistribution study was performed in female nude mice (*n* = 12) including both healthy animals (*n* = 9) and MDA-MB-231 tumour-bearing mice (*n* = 3). These animals were injected with 30–37 MBq of the radiolabelled uPA activity-based probe [¹¹¹In]MICA-401 via the lateral tail vein. At 30 min, 2 h and 18 h post injection, each time three healthy animals were sacrificed by cervical dislocation and an *ex vivo* biodistribution was performed. The tumour-bearing animals underwent longitudinal static SPECT scans (cfr. *infra*) at 2 h, 4 h, 18 h and 95 h post injection and were sacrificed at the end of the last scan. Blood was collected via cardiac puncture and the main organs were thereafter rapidly removed and rinsed in PBS. Radioactivity in the samples was measured using an automatic gamma counter (2480 WIZARD2, Perkin Elmer) and expressed as a percentage of the injected dose per gram of tissue plus or minus the standard deviation (%ID/g ± SD).

2.6. Imaging study with active and hydrolysed [¹¹¹In]-labelled uPA activity-based probe

µSPECT/CT scans of the uPA activity-based probe [¹¹¹In]MICA-401 were performed in HT-29 (*n* = 5), MDA-MB-231 (*n* = 5) and healthy control groups (*n* = 5). Similarly, µSPECT/CT scans with the hydrolysed inactive uPA probe [¹¹¹In]MICA-402 were also performed in HT-29 (*n* = 5) and MDA-MB-231 (*n* = 5) groups. These static SPECT scans were acquired 95 h post injection, and *ex vivo* biodistribution, as described above, was additionally acquired. The radiotracer was injected in the lateral tail vein, with an average of 20.35 ± 8.14 MBq (9.41 ± 3.36 GBq/µmol) for [¹¹¹In]MICA-401, and 35.15 ± 4.81 MBq (specific activity not determined for inactive probe) for [¹¹¹In]MICA-402, depending on the

yield of each radiosynthesis. The μ SPECT scans had durations of 30, 45 or 90 min, depending on the absolute injected dose, to obtain similar signal-to-noise ratios in the reconstructed images for every performed μ SPECT scan. To undergo the scan procedure, animals were anaesthetized with isoflurane (3–5% for induction, 1–2% for maintenance). Further, all mice were scanned on a VECTOR system (MILabs, Utrecht, The Netherlands) with the animal bed translated in three dimensions using an XYZ stage. A 20% main photopeak was centred at 171 and 245 keV to reconstruct the ^{111}In images on 1.2 mm^3 voxels by 20 iterations of 16 POSEM (pixel-based ordered-subset expectation maximization) subsets. For whole body imaging, eight bed positions were used with a head first prone orientation and anatomical CT images were acquired (45 kV, 615 μA). Regions of interest (ROIs) were drawn on the CT images manually in PMOD software 3.3 (PMOD technologies, Zürich, Switzerland). Subsequently, tracer uptake was expressed as %ID/g tissue and as mean standardized uptake value (SUV), which was generated by summation of voxels within the tomographic planes. SUV was defined as $(\text{CT} \times W)/D_{\text{inj}}$, where CT is radioactivity counts in the tissue (kBq/cm^3), W is the weight of the animal (g) and D_{inj} is injected dose (kBq). A technical consideration to make is that, despite the differences in tumour volumes between the two different xenograft models (150 versus 450 mm^3), the smallest tumour diameter (i.e. around 4 mm) is four times the resolution of the scanner (i.e. around 1 mm), hereby excluding partial volume effects. Therefore, no signal recovery differences are to be expected between the different tumour diameters.

2.7. Validation by anti-human uPA ELISA and ex vivo histology

The human uPA protein level of both models was determined in the tumour tissue ($n=5$ for MDA-MB-231 and $n=5$ for HT-29) using ELISA. Therefore, at the end of each scan of the aforementioned imaging study, tumour tissue was collected and part of the tumour was snap-frozen in liquid nitrogen and stored at -80°C until analysis. The remaining part of the tumour was used

for histological examination. All tumour tissues were homogenized for ELISA analysis using a gentleMACS tissue dissociator (Miltenyi Biotec, North Ryde, New South Wales, Australia). Total protein content of the tumour tissue samples was measured using a BCA protein assay kit (Thermo Fisher Scientific, Waltham, MA, USA) according to the protocol provided. The total human uPA content was measured using the IMUBIND® uPA ELISA kit (American Diagnostica, Stamford, CT, USA) according to the manufacturer's instructions and normalized to the total protein content of the tumour lysates ($\text{ng uPA}/\text{mg protein}$).

The remainder of all tumours ($n=20$) and lymph nodes (LNs; inguinal, $n=23$; axillary, $n=24$) were excised and fixed in formalin. Immunohistochemistry (IHC) was performed using two different primary rabbit polyclonal antibodies, one targeting specific human (ab24121, Abcam, Cambridge, UK) and a second one targeting specific mouse uPA (LS-C150831, LifeSpan BioSciences, Seattle, WA, USA). Negative control sections were processed identically, except for the lack of the primary antibody. A human prostate carcinoma slide and a mouse pancreatic carcinoma (with confirmed uPA expression) was used as positive control for human and mouse uPA immunostaining respectively and to evaluate species cross-reactivity of both uPA-targeting antibodies. In addition, to investigate the proliferation status of the tumours and to detect human tumour cells in mouse lymph nodes (micro-metastases) a rabbit polyclonal antibody was used targeting human Ki67 (no 12202, Cell Signaling Technology, Danvers, MA, USA). A tumour slide (already stained positively for Ki67) was included as positive control tissue. A description of the protocol and scoring system is provided in the supplementary data.

2.8. Statistical analysis

GraphPad Prism 6.0c (GraphPad, La Jolla, CA, USA) was applied for all statistical analysis. To verify if the data were normally distributed, a Shapiro–Wilk normality test was applied. Differences between the biodistribution groups were statistically evaluated by one-way ANOVA and Tukey's multiple comparison test.

Table 1. *In vitro* evaluation of compounds uPA-PET (28) and MICA-401 as well as negative control compound MICA-402

| | | IC_{50} (μM) | |
|------------|---|---|-----------------------------|
| | PET probe (28) | SPECT probe (MICA-401) | Hydrolysed probe (MICA-402) |
| Human uPA | $0.019 \pm 0.002^{**}$ $k_{\text{app}} = 6.80 \times 10^3 \pm 0.25 \times 10^3/(\text{M s})$ | $0.022 \pm 0.002^{**}$ $k_{\text{app}} = 4.80 \times 10^3 \pm 0.32 \times 10^3/(\text{M s})$ | >10 |
| Mouse uPA | $0.858 \pm 0.056^{**}$ $k_{\text{app}} = 1.46 \times 10^2 \pm 0.11 \times 10^2/(\text{M s})$ | $1.29 \pm 0.08^{**}$ $k_{\text{app}} = 1.19 \times 10^2 \pm 0.95 \times 10^2/(\text{M s})$ | >25 |
| tPA | 46.1 ± 4.6 | >10 | >10 |
| Thrombin | 13.2 ± 0.6 | >10 | >250 |
| Plasmin | 5.9 ± 0.8 | >10 | >250 |
| FXa | 62 | >10 | >10 |
| Plasma KLK | >2.5 | >10 | >10 |
| KLK1 | >10 | >10 | >10 |
| KLK4 | $0.013 \pm 0.001^*$ | $0.036 \pm 0.003^*$ | >25 |
| KLK8 | $0.050 \pm 0.004^*$ | $0.033 \pm 0.004^*$ | >2.5 |
| HNE | >2.5 | >2.5 | >10 |
| ACHE | >20 | >20 | >20 |

*Reversible binding kinetics.
**Irreversible binding kinetics.

Differences between two unpaired independent groups were analysed with a non-parametric Mann–Whitney *U*-test. For a correlation study, a non-parametric Spearman test was performed. Data are reported as mean \pm SEM and $p < 0.05$ was considered statistically significant.

3. RESULTS

3.1. Chemistry and *in vitro* evaluation

The cold standard MICA-401 was synthesized in two steps starting from the amine **2** (Fig. S1) (28). In the first step, the addition of the DOTA chelator was achieved in a moderate yield (42%, Fig. S1) and gave access to precursor **3**. Complexation of the DOTA ring with InCl_3 led to the standard MICA-401, also in moderate yield (42%). The same synthetic strategy was applied to prepare compounds **5** and MICA-402 after hydrolysis of amine **2** (Fig. S2). Both compounds MICA-401 and MICA-402 were evaluated *in vitro* to determine their affinity for uPA (human and mouse) and for a panel of nine related serine proteases and AChE. The uPA SPECT probe MICA-401 appeared to be a potent, selective and irreversible uPA inhibitor ($k_{\text{app}} = 4.80 \times 10^3 / (\text{M s})$ for human uPA) while the hydrolysed probe MICA-402 lost all affinity for uPA (Table 1), as anticipated. In conclusion, the SPECT probe MICA-401 is able to make a covalent bond selectively with uPA compared with a broad panel of related enzymes, and therefore should allow the selective imaging of uPA activity *in vivo*. Since the hydrolysed compound MICA-402 shows no binding to any of the enzymes, this compound is well suited to serve as negative control to demonstrate that the observed imaging is not due to any aspecific interaction.

3.2. Radiochemistry

The radiosynthesis of $[^{111}\text{In}]\text{MICA-401}$ and $[^{111}\text{In}]\text{MICA-402}$ was performed by complexation of $[^{111}\text{In}]\text{InCl}_3$ at 60 °C for 45 min (Fig. 2). The crude reaction mixture was purified by analytical HPLC. The column was eluted with a biocompatible mobile phase (0.05 M NaOAc, pH 5.5/EtOH) and the collected radiotracer was filtered through a sterile filter and diluted with a sterile solution of 0.9% NaCl to reduce the ethanol concentration to below 10% for *in vivo* evaluation. $[^{111}\text{In}]\text{MICA-401}$ and $[^{111}\text{In}]\text{MICA-402}$ were respectively produced with an average radiochemical conversion of 90% ($n = 4$) and 92% ($n = 2$). After purification and formulation the yields dropped to 49% ($n = 4$) for $[^{111}\text{In}]\text{MICA-401}$ and 71% ($n = 2$) for $[^{111}\text{In}]\text{MICA-402}$. The radiochemical purity was above 95% and the tracers were stable in solution for at least 5 h post radiosynthesis as determined by HPLC analysis.

3.3. Time window selection

The radiotracer $[^{111}\text{In}]\text{MICA-401}$ slowly cleared from the blood of healthy animals, with $7.54 \pm 0.78\% \text{ID/g}$ still present at 18 h post injection. Clearance was mainly through the renal system, with a kidney uptake of $7.14 \pm 0.77\% \text{ID/g}$ at 30 min post injection, decreasing to $2.59 \pm 0.31\% \text{ID/g}$ at 18 h post injection (Fig. 3). Other organs showing moderate tracer uptake were lungs, liver, spleen and skin. Pancreas, stomach, small and large intestine, muscle, bone and brain showed negligible uptake ($< 4\% \text{ID/g}$) at any of the time points. Further, *ex vivo* biodistribution of tumour-bearing animals 95 h post injection indicated an almost complete clearance from the blood ($1.40 \pm 0.35\% \text{ID/g}$). Uptake was seen in the liver ($7.10 \pm 1.15\% \text{ID/g}$), spleen ($5.87 \pm 0.19\% \text{ID/g}$),

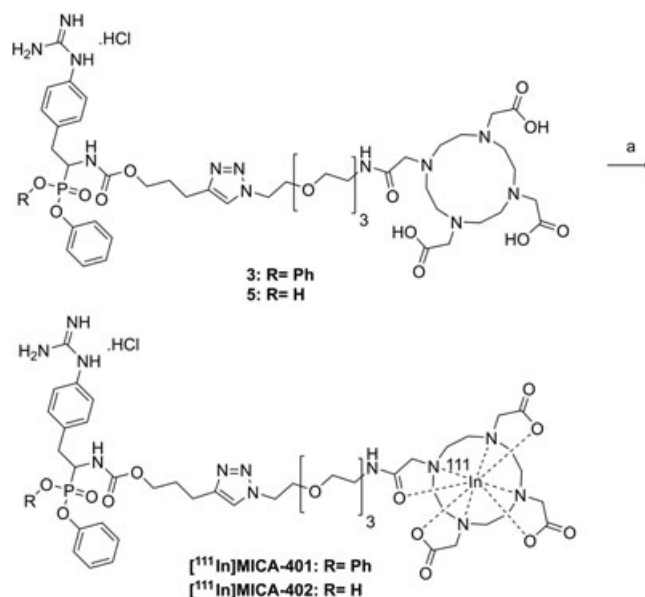


Figure 2. Radiosynthesis of $[^{111}\text{In}]\text{MICA-401}$ and $[^{111}\text{In}]\text{MICA-402}$. Reagents and conditions: a, $[^{111}\text{In}]\text{InCl}_3$, 0.5 M NH_4OAc , pH 5.5, 45 min at 60 °C, 49–71%.

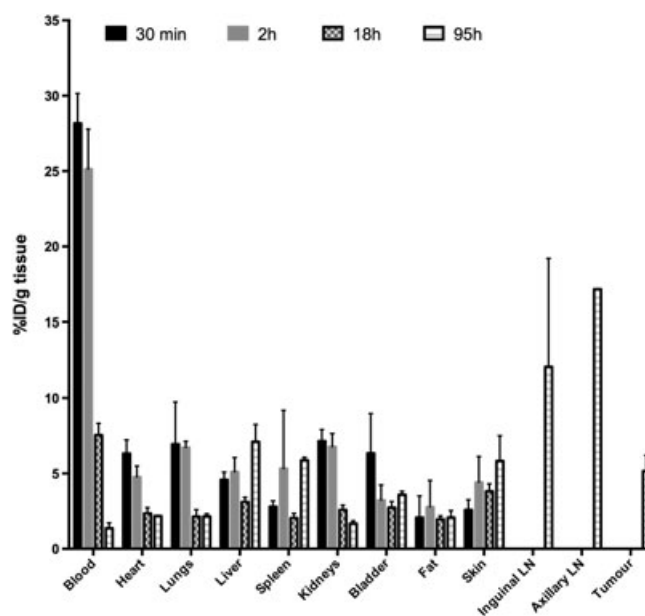


Figure 3. *Ex vivo* biodistribution of $[^{111}\text{In}]\text{MICA-401}$ at different time points post injection in healthy and tumour-bearing mice. Data from adjacent LN, axillary LN and tumours were only collected at 95 h post injection. Results are shown as mean \pm SD ($n = 3/\text{group}$).

skin ($5.83 \pm 1.67\% \text{ID/g}$) and adjacent ($12.08 \pm 7.13\% \text{ID/g}$) and axillary ($17.17\% \text{ID/g}$, $n = 1$) LNs. Tumour uptake was $5.16 \pm 1.04\% \text{ID/g}$ (Fig. 3).

SPECT images in Fig. 4 show good tumour visualization from 18 h post injection onwards, with a more pronounced radiotracer uptake in the rim of the tumour. The optimal tumour contrast is reached at the 95 h post injection time point. High uptake by skin and active drainage to and uptake by lymph nodes are also clearly visible (Fig. 4).

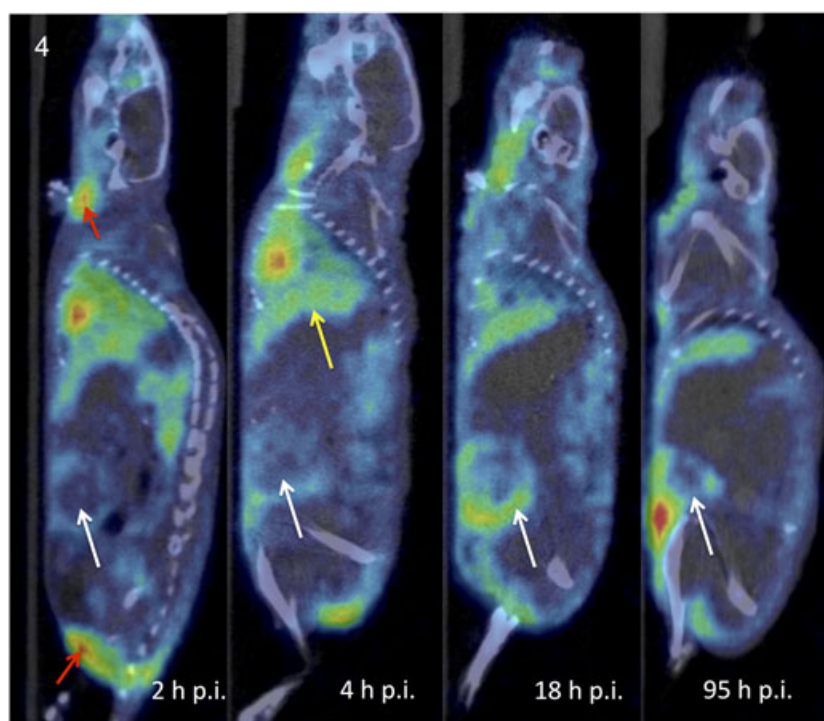


Figure 4. Representative SPECT images of an MDA-MB-231-bearing mouse longitudinally imaged with the activity-based uPA probe [^{111}In]MICA-401. Sagittal images at the different time points (2 h, 4 h, 18 h and 95 h post injection). The white arrows indicate tumours, the yellow arrow indicates liver and the red arrows indicate active drainage to lymph nodes (axillary and inguinal). SUV scale from 0 to 2.

3.4. *In vivo* imaging study

Post-scan *ex vivo* biodistribution in healthy control animals, as well as the MDA-MB-231 and HT29 groups, showed comparable tracer distributions of the uPA inhibitor [^{111}In]MICA-401, with high uptake in the liver ($5.55 \pm 1.01\% \text{ID/g}$), spleen ($4.50 \pm 1.22\% \text{ID/g}$) and skin ($6.22 \pm 1.20\% \text{ID/g}$) as averaged over the three groups (Fig. 5). High tumour uptake ($5.68 \pm 1.41\% \text{ID/g}$ and $5.43 \pm 1.29\% \text{ID/g}$) in the MDA-MB-231 and HT-29 models, respectively, was demonstrated. Also, a remarkably high uptake was observed in the LNs for all animals, up to $12.21 \pm 6.70\% \text{ID/g}$ in the inguinal LNs of the MDA-MB-231 group.

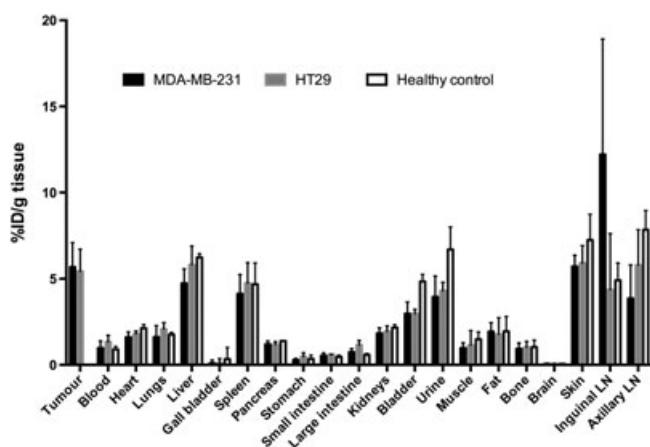


Figure 5. *Ex vivo* biodistribution of the uPA activity-based probe [^{111}In]MICA-401 at 95 h post injection in MDA-MB-231, HT-29 and healthy mice. Results are shown as mean \pm SD ($n = 5/\text{group}$).

In vivo SPECT images for [^{111}In]MICA-401 are shown in Fig. 6. Both tumour types are easily detectable and moderate tumour uptake was observed for the MDA-MB-231 and HT-29 models: 1.18 ± 0.18 and 1.10 ± 0.29 respectively for mean SUV, and 4.33 ± 0.80 and 4.86 ± 1.18 respectively for $\% \text{ID/g}$. Uptake of [^{111}In]MICA-401 in liver, LNs and skin was also confirmed on the SPECT images. Further, a high and significant correlation was obtained between the *in vivo* measured tumour SUVs and the *ex vivo* $\% \text{ID/g}$ tumour tissue ($r = 0.6070$, $p = 0.0214$).

For the hydrolysed inactive uPA probe, [^{111}In]MICA-402, an almost complete removal from the mouse body was observed *ex vivo* and *in vivo* (Fig. 7A, B respectively) 95 h post injection, as uptake in all organs was less than $1\% \text{ID/g}$. Further, these SPECT images equally indicated a renal clearance of [^{111}In]MICA-402. As anticipated, no tumours could be detected with this hydrolysed inactive uPA probe (Fig. 7B).

3.5. *Ex vivo* validation

uPA levels determined by ELISA in both tumour types showed a significantly higher human uPA expression in MDA-MB-231 tumour samples ($21.42 \pm 3.40 \text{ ng uPA/mg protein}$) compared with HT-29 tumours ($1.96 \pm 0.36 \text{ ng uPA/mg protein}$, $p < 0.0001$).

Target specificity and species specificity for both anti-human and anti-mouse uPA antibodies were investigated. The positive control tissue (human prostate carcinoma) for anti-human uPA showed a clear, specific uPA staining pattern of the glands, while the negative control without the primary antibody proved no background staining. The positive control tissue (mouse pancreatic carcinoma) for the anti-mouse uPA antibody showed clear and specific uPA staining while the negative control showed only a slight background staining. Investigating possible cross-reactivity,

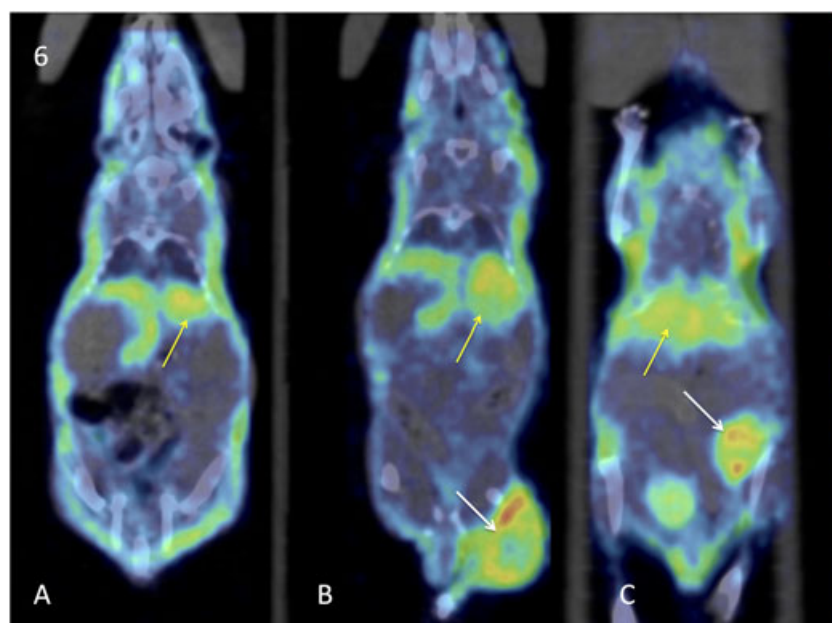


Figure 6. Representative SPECT images at 95 h post injection of the uPA activity-based probe [^{111}In]MICA-401 in the three models. (A) Healthy control mouse; (B) HT-29 tumour-bearing mouse; (C) MDA-MB-231 tumour-bearing mouse. The white arrows indicate tumours and yellow arrows indicate liver. All images scaled to the same colour scale (SUV scale from 0 to 2).

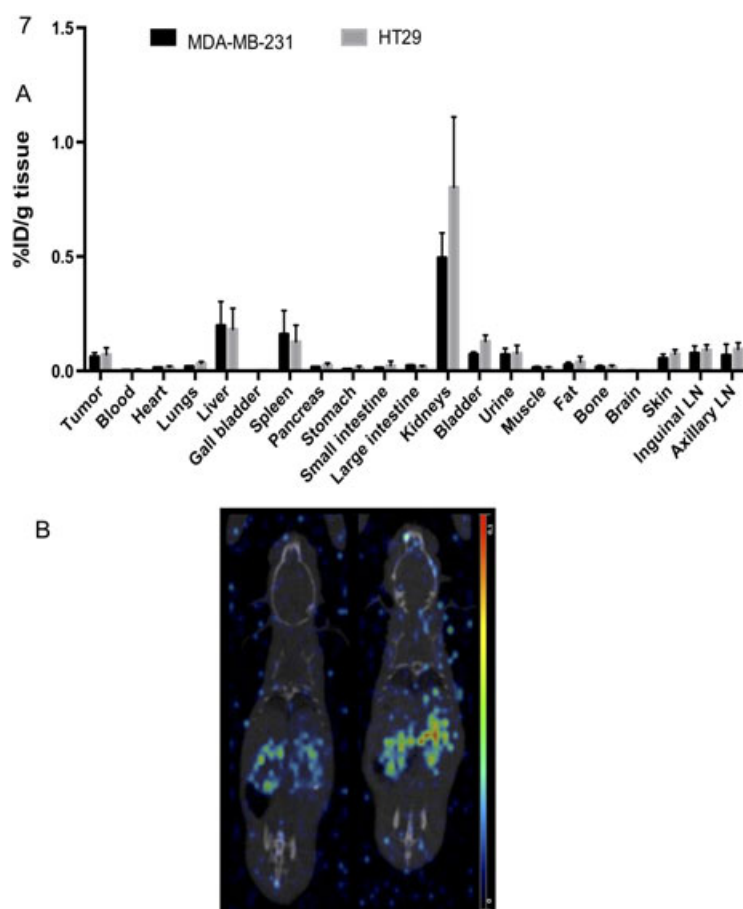


Figure 7. *Ex vivo* biodistribution and a representative SPECT image at 95 h post injection of the hydrolysed, inactive uPA probe [^{111}In]MICA-402. (A) *Ex vivo* biodistribution data of MDA-MB-231 and HT-29 tumour-bearing mice. Results are shown as mean \pm SD ($n = 5/\text{group}$). (B) SPECT image of HT-29 (left) and MDAMB-231 (right) tumour-bearing mice imaged 95 h post injection of the inactive radiotracer. Both images scaled to the same colour scale (SUV scale from 0 to 0.1).

staining of the mouse uPA positive control tissue with the anti-human uPA antibody did however show weak staining of tumour cells and staining of mouse lymphoid cells and macrophages, so species cross-reactivity occurs with the anti-human uPA antibody. Moreover, staining of the human prostate carcinoma tissue with the anti-mouse uPA antibody demonstrated a clear staining pattern comparable to that of the human uPA staining, confirming species cross-reactivity of this antibody as well; however, staining differences were still present when human antibodies were compared with mouse uPA and vice versa.

The two tumour types showed a clear staining with the anti-human uPA antibody in both MDA-MB-231 and HT-29 tumours. An overall, high staining was observed in the MDA-MB-231 tumours, with both pericellular and intracellular staining of tumour cells, staining positively over the entire section of the tumours. By morphological criteria tumoral stroma and some macrophages also showed uPA immunoreactivity (Fig. 8A, B). In the HT-29 tumours a weaker staining pattern was observed (which is in line with the ELISA data), with primarily granulated pericellular uPA staining with a more pronounced staining at the rim of the tumours (Fig. 8D, E). No (or little) stromal uPA staining and no intracellular staining of the tumour cells were observed. IHC scores for the MDA-MB-231 were significantly higher compared with HT-29 scores (Fig. 9, $p = 0.008$).

Staining with the anti-mouse antibody revealed a more comparable staining intensity and pattern between the two tumour types (Fig. 8C, F). In the MDA-MB-231 tumours a more heterogeneous staining pattern could be observed with a mix of intense and negative stained regions in the tumours. uPA immunoreactivity was found intracellularly, in tumoral stroma and in macrophages. In the HT29 tumours, a typical granulated, pericellular staining was again observed, with more stromal staining compared with the anti-human uPA antibody. Macrophages and some endothelial cells also showed positive uPA staining. No significant differences were demonstrated between the IHC scores (Fig. 9).

Due to the high LN uptake measured *ex vivo* and *in vivo* using the SPECT images, LN sections were also stained with H&E and antibody directed to human Ki67 was used to identify micrometastases. No Ki67 staining was visible and also no micrometastasis could be revealed on the H&E-stained LN

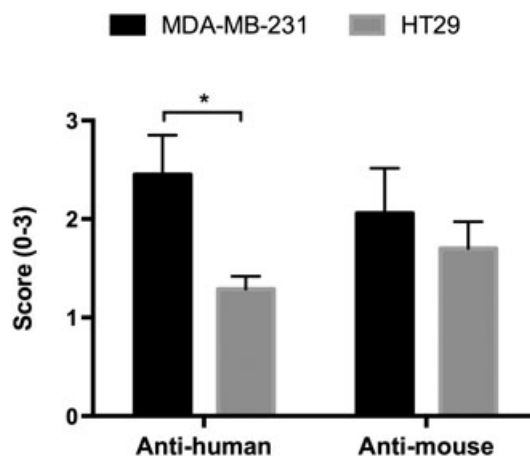


Figure 9. IHC scores of human and mouse uPA of both tumour models. Grading was performed by two independent observers and as described in the materials and methods section. The difference in score between the two tumour models is significant for the anti-human uPA staining ($p = 0.008$), but not for the anti-mouse uPA staining.

sections. In addition, LNs showed clear anti-mouse uPA staining in the medulla of the LN, where – among other cell types – histiocytes, macrophages and dendritic cells are present (Fig. S3A–C). More remarkable is the intense uPA staining of the surrounding brown adipose tissue, sometimes present on the dissected LN sections. A strong, specific staining of the adipocytes, small blood vessels and macrophages present in the brown fat is illustrated in Fig. S3A, D.

4. DISCUSSION

Our objective is to develop a molecular imaging probe for discrimination between high and low uPA activity in tumours with a view to prediction of tumour invasiveness, therapeutic intervention and personalized treatment (20–23). In a previous study with [^{18}F]1 (Fig. 1) (28), we observed an unfavourable stability profile combined with slow blood clearance. Scanning at later time points increases the tumour/blood ratio of the uPA activity

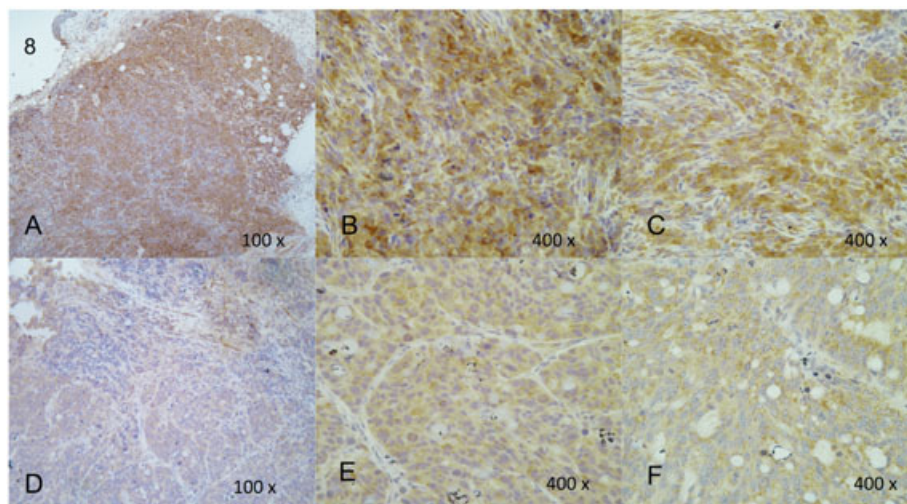


Figure 8. IHC staining of human and mouse uPA in tumour sections. (A, B) MDA-MB-231 tumour stained for human uPA, (C) MDA-MB-231 tumour stained for mouse uPA, (D, E) HT-29 tumour stained for human uPA, (F) HT-29 tumours stained for mouse uPA.

based probe, and therefore ^{111}In -indium with a half-life of 2.80 days was selected to design a SPECT probe. The aforementioned PET probe showed a similar inactivation rate constant (k_{app}) for human uPA ($k_{\text{app}} = 6.80 \times 10^3 \pm 0.25 \times 10^3 / (\text{Ms})$) to the current SPECT probe, MICA-401 ($k_{\text{app}} = 4.80 \times 10^3 \pm 0.32 \times 10^3 / (\text{Ms})$), whereas both probes had 40-fold reduced inactivation rate constants for mouse uPA (Table 1). Both the SPECT probe MICA-401 and the PET probe demonstrated similar affinities for two closely related trypsin-like proteases, kallikrein (KLK)4 and KLK8, compared with uPA. However, rigorous analysis of the binding kinetics showed that the binding to KLK4 and KLK8 is reversible. This is a further demonstration that potent binding of a molecule with a warhead designed to be irreversible does not always result in irreversible binding (30).

Our *ex vivo* and *in vivo* biodistribution data with the uPA activity-based probe [^{111}In]MICA-401 demonstrated a high blood activity 18 h post injection (about 7%ID/g), which declined to approximately 1%ID/g at 95 h post injection. At this time point, tumours were clearly detectable and *ex vivo* biodistribution indicated MDA-MB-231 tumour uptake of approximately 5%ID/g. Therefore, 95 h post injection was chosen as the ideal imaging time point for further experiments. Compared with our previously developed [^{18}F]1 (Fig. 1) radiotracer, the uPA activity-based probe [^{111}In]MICA-401 showed substantially lower uptake in the large intestines and blood, while a higher liver and spleen activity was observed (28). In the MDA-MB-231 model we found a tumour uptake *ex vivo* of 5.7%ID/g and *in vivo* of 4.3%ID/g, while we obtained a relatively low tumour uptake with our previous [^{18}F]1 uPA probe (peak uptake of 2.4%ID/g *ex vivo* and 2.5%ID/g *in vivo* at 4 h post injection) (28). A direct comparison of the quantitative tumour uptake between previous published studies targeting uPAR (23–25,34) is not feasible, as in our study enzymatically active uPA is targeted and quantified. Recently, an ^{111}In -labelled U33, an antibody directed to uPA, showed a remarkable tumour uptake of 43.2%ID/g 72 h post injection in a prostate cancer xenograft, which was attributed to the internalization through an uPAR mediated mechanism (35).

A similar uptake of [^{111}In]MICA-401 was observed for both tumour models *ex vivo* as well as *in vivo*, despite the known differential *in vitro* uPA expression between the two cell lines. Additionally, uPA ELISA and IHC using the anti-human uPA antibody performed on tumour tissue revealed a significant higher human uPA expression of the MDA-MB-231 model than the HT-29 model. However, IHC staining with the anti-mouse uPA antibody on the tumour sections showed no significant difference in mouse uPA expression between the tumour types, suggesting that mouse uPA levels were more comparable. Nevertheless, caution should be taken in the interpretation of these IHC data as we demonstrated species cross-reactivity of both uPA-targeting antibodies. This discrepancy of *in vitro* and *in vivo* uPA expression has already been demonstrated by Hsiao *et al.*, who evaluated uPA sensitive fluorescence imaging probes in two different models, including the HT-29 and a high uPA expression fibrosarcoma model. Similar fluorescence intensities in the two models were observed, and it was hypothesized that HT-29 tumour cells need to recruit host uPA expressed by neighbouring stroma cells through their surface uPAR to grow *in vivo* (36). In this case, the amount of active uPA may be similar in the two models, but therefore not the antigen levels (pro-uPA plus uPA). Another point to consider is the possible binding of the uPA SPECT probe to other serine proteases present in tumours. However, we demonstrated in an *in vitro* panel of highly

related serine proteases that the SPECT probe MICA-401 can only bind covalently to human and mouse uPA. Since imaging is performed at 95 h post injection it is highly unlikely that any non-covalently bound probe is still present. This is confirmed by the absence of the inactivated probe MICA-402 at 95 h post injection, which we confirmed is unable to make covalent bonds to the tested serine proteases.

Remarkably, a very high uptake was also observed in the LNs in both cancer models and the healthy control group. Both H&E and staining with a specific anti-human Ki67 antibody were thoroughly analysed, but no proliferating human tumour cells could be detected in the mouse LNs, excluding the presence of micrometastases. Immunohistochemical staining with anti-mouse uPA of all the LNs revealed specific uPA presence in the cortex and medulla of the LNs, and in particular histiocytes, macrophages and dendritic cells stained positively. Notably, an intense uPA staining of the brown fat, occasionally present on the section of the dissected LNs, was present. A specific staining of the adipocytes and small blood vessels in the adipose tissue was visible. Indeed, high expression levels of PAI-1 and uPA have been described in adipocyte tissue, and furthermore uPAR is known to be preferentially expressed in infiltrating adipose tissue macrophages (37,38).

5. CONCLUSION

We have synthesized and characterized an ^{111}In -labelled activity-based SPECT probe that selectively targets active uPA, and we have proven its usefulness in two xenograft mouse models. Moderate tumour uptake was found in both tumour models with clear, detectable tumours on μSPECT images at 95 h post injection. The high uptake in non-invaded lymph nodes reported here may represent a limitation to the clinical translation of this tracer for oncological applications. Therefore, translational capabilities of this [^{111}In]MICA-401 radiotracer for future clinical cancer patient management remains to be further explored.

Acknowledgements

This work was supported by the Special Fund for Research of the University of Antwerp (BOF-UA), the Industrial Research Fund of the University of Antwerp (IOF-UA), the Agency for Innovation by Science and Technology (IWT) with a Strategic Basic Research (SBO) grant (ChemProTools) and an Innovation Mandate (Jurgen Joossens), the Hercules Foundation Flanders with medium-scale research infrastructure grants and the Research Foundation Flanders (FWO) with a research project (G013513N). The Laboratory of Medicinal Chemistry belongs to the Department of Pharmaceutical Sciences and is a partner of the Antwerp Drug Discovery Network (www.ADDN.be). The Molecular Imaging Center Antwerp belongs to the Faculty of Medicine and Health Science. The excellent technical assistance of Sophie Lyssens, Ingmar Stuyver, Philippe Joye and Mathias Van Den Eynde is greatly appreciated.

This work was also funded by Antwerp University Hospital, Belgium, through a postdoctoral position for Christel Vangestel (Innovative Medicines Initiative, Quick-Concept), a full-time position for Leonie Wyffels and a departmental position for Patrick Pauwels and Sigrid Stroobants.

We would also like to thank the Laboratory of Cell Biology and Histology, University of Antwerp (Professor Jean-Pierre Timmermans) for providing the gentleMACS tissue dissociator at their facility.

REFERENCES

- Shimizu M, Cohen B, Goldvasser P, Berman H, Virtanen C, Reedijk M. Plasminogen activator uPA is a direct transcriptional target of the JAG1–Notch receptor signaling pathway in breast cancer. *Cancer Res* 2011; 71: 277–286.
- Choong PF, Nadesapillai AP. Urokinase plasminogen activator system: a multifunctional role in tumor progression and metastasis. *Clin Orthop Relat Res* 2003; 415: S46–58.
- Mengele K, Napieralski R, Magdolen V, Reuning U, Ghazepis A, Sweep F, Brünner N, Foekens J, Harbeck N, Schmitt M. Characteristics of the level-of-evidence-1 disease forecast cancer biomarkers uPA and its inhibitor PAI-1. *Expert Rev Mol Diagn* 2010; 10: 947–962.
- Tang L, Han X. The urokinase plasminogen activator system in breast cancer invasion and metastasis. *Biomed Pharmacother* 2013; 67: 179–182.
- Andreasen PA, Egelund R, Petersen HH. The plasminogen activation system in tumor growth, invasion, and metastasis. *Cell Mol Life Sci* 2000; 57: 25–40.
- Duffy MJ, Duggan C, Mulcahy HE, McDermott EW, O'Higgins NJ. Urokinase plasminogen activator: a prognostic marker in breast cancer including patients with axillary node-negative disease. *Clin Chem* 1998; 44: 1177–1183.
- Look MP, van Putten WL, Duffy MJ, Harbeck N, Christensen IJ, Thomssen C, Kates R, Spyros F, Fernö M, Eppenberger-Castori S, Sweep C, Peyrat J-P, Martin PM, Magdelenat H, Brünner N, Duggan C, Lisboa BW, Bendahl PO, Quillien V, Daver A, Ricolleau G, Meijer-van Gelder ME, Manders P, Fiets FW, Blankenstein MA, Broët P, Romain S, Daxenbichler G, Windbichler G, Cufer T, Borstnar S, Kueng W, Beex LV, Klijn JG, O'Higgins N, Eppenberger U, Jänicke F, Schmitt M, Foekens JA. Pooled analysis of prognostic impact of urokinase-type plasminogen activator and its inhibitor PAI-1 in 8377 breast cancer patients. *J Natl Cancer Inst* 2002; 94: 116–128.
- Harbeck N, Kates RE, Gauger K, Willems A, Kiechle M, Magdolen V, Schmitt M. Urokinase-type plasminogen activator (uPA) and its inhibitor PAI-1: novel tumor-derived factors with a high prognostic and predictive impact in breast cancer. *Thromb Haemost* 2004; 91: 450–456.
- Annecke K, Schmitt M, Euler U, Zerm M, Paepke D, Paepke S, von Minckwitz G, Thomssen C, Harbeck N. uPA and PAI-1 in breast cancer: review of their clinical utility and current validation in the prospective NNBC-3 trial. *Adv Clin Chem* 2008; 45: 31–45.
- Andres SA, Edwards AB, Wittliff JL. Expression of urokinase-type plasminogen activator (uPA), its receptor (uPAR), and inhibitor (PAI-1) in human breast carcinomas and their clinical relevance. *J Clin Lab Anal* 2012; 26: 93–103.
- Oka T, Ishida T, Nishino T, Sugimachi K. Immunohistochemical evidence of urokinase-type plasminogen activator in primary and metastatic tumors of pulmonary adenocarcinoma. *Cancer Res* 1991; 51: 3522–3525.
- Sheng S. The urokinase-type plasminogen activator system in prostate cancer metastasis. *Cancer Metastasis Rev* 2001; 20: 287–296.
- Kuhn W, Schmalfeldt B, Reuning U, Pache L, Berger U, Ulm K, Harbeck N, Späthe K, Dettmar P, Höfler H, Jänicke F, Schmitt M, Graeff H. Prognostic significance of urokinase (uPA) and its inhibitor PAI-1 for survival in advanced ovarian carcinoma stage FIGO IIIc. *Br J Cancer* 1999; 79: 1746–1751.
- Kobayashi H, Fujishiro S, Terao T. Impact of urokinase-type plasminogen activator and its inhibitor type 1 on prognosis in cervical cancer of the uterus. *Cancer Res* 1994; 54: 6539–6548.
- Gorantla B, Asuthkar S, Rao JS, Patel J, Gondi CS. Suppression of the uPAR-uPA system retards angiogenesis, invasion, and in vivo tumor development in pancreatic cancer cells. *Mol Cancer Res* 2011; 9: 377–389.
- Mulcahy H, O'Donoghue D, Duffy M. Urokinase-type plasminogen activator and outcome in Dukes' B colorectal cancer. *Lancet* 1994; 583–584.
- Nekarda H, Schmitt M, Ulm K, Wenninger A, Vogelsang H, Becker K, Roder JD, Fink U, Siewert JR. Prognostic impact of urokinase-type plasminogen activator and its inhibitor PAI-1 in completely resected gastric cancer. *Cancer Res* 1994; 54: 2900–2907.
- Benraad TJ, Geurts-Moespot J, Grøndahl-Hansen J, Schmitt M, Heuvel JJ, de Witte JH, Foekens JA, Leake RE, Brünner N, Sweep CG. Immunoassays (ELISA) of urokinase-type plasminogen activator (uPA): report of an EORTC/BIOMED-1 workshop. *Eur J Cancer* 1996; 32A: 1371–1381.
- Michalski MH, Chen X. Molecular imaging in cancer treatment. *Eur J Nucl Med Mol Imaging* 2010; 38: 358–377.
- Backer MV, Backer JM. Imaging key biomarkers of tumor angiogenesis. *Theranostics* 2012; 2: 502–515.
- Duffy MJ, Crown J. A personalized approach to cancer treatment: how biomarkers can help. *Clin Chem* 2008; 54: 1770–1779.
- Prechtel A, Harbeck N, Thomssen C, Meisner C, Braun M, Untch M, Wieland L, Lisboa B, Cufer T, Graeff H, Selbmann K, Schmitt M, Jänicke F. Tumor biological factors uPA and PAI-1 as stratification criteria of a multicenter adjuvant chemotherapy trial in node-negative breast cancer. *Int J Biol Markers* 2000; 15: 73–78.
- Liu D, Overbey D, Watkinson L, Giblin MF. Synthesis and characterization of an ¹¹¹In-labeled peptide for the in vivo localization of human cancers expressing the urokinase-type plasminogen activator receptor (uPAR). *Bioconjugate Chem* 2009; 20: 888–894.
- Li ZB, Niu G, Wang H, He L, Yang L, Ploug M, Chen X. Imaging of urokinase-type plasminogen activator receptor expression using a ⁶⁴Cu-labeled linear peptide antagonist by microPET. *Clin Cancer Res* 2008; 14: 4758–4766.
- Persson M, Madsen J, Østergaard S, Jensen MM, Jørgensen JT, Juhl K, Lehmann C, Ploug M, Kjaer A. Quantitative PET of human urokinase-type plasminogen activator receptor with ⁶⁴Cu-DOTA-AE105: implications for visualizing cancer invasion. *J Nucl Med* 2012; 53: 138–145.
- Bekes EM, Deryugina EI, Kupriyanova TA, Zajac E, Botkjaer KA, Andreasen PA, Quigley JP. Activation of pro-uPA is critical for initial escape from the primary tumor and hematogenous dissemination of human carcinoma cells. *Neoplasia* 2011; 13: 806–821.
- Persson M, Skovgaard D, Brandt-Larsen M, Christensen C, Madsen J, Nielsen CH, Thurison T, Klausen TL, Holm S, Loft A, Berthelsen AK, Ploug M, Pappot H, Brasso K, Kroman N, Hojgaard L, Kjaer A. First-in-human uPAR PET: imaging of cancer aggressiveness. *Theranostics* 2015; 5: 1303–1316.
- Ides J, Thomae D, Wyffels L, Vangestel C, Messagie J, Joossens J, Lardon F, Van der Veken P, Agustyns K, Stroobants S, Staelens S. Synthesis and in vivo preclinical evaluation of an ¹⁸F labeled uPA inhibitor as a potential PET imaging agent. *Nucl Med Biol* 2014; 41: 477–484.
- Joossens J, Ali OM, El-Sayed I, Surpateanu G, Van der Veken P, Lambeir A-M, Setyono-Han B, Foekens JA, Schneider A, Schmalix W, Haemers A, Augustyns K. Small, potent, and selective diaryl phosphonate inhibitors for urokinase-type plasminogen activator with in vivo antimetastatic properties. *J Med Chem* 2007; 50: 6638–6646.
- Gladysz R, Adriaenssens Y, De Winter H, Joossens J, Lambeir AM, Augustyns K, Van der Veken P. Discovery and SAR of novel and selective inhibitors of urokinase plasminogen activator (uPA) with an imidazo[1,2-a]pyridine scaffold. *J Med Chem* 2015; 6: 1954–1958.
- van Soom J, Crucitti GC, Gladysz R, van der Veken P, Di Santo R, Stuyver I, Buck V, Lambeir AM, Magdolen V, Joossens J, Augustyns K. The first potent diphenyl phosphonate KLK4 inhibitors with unexpected binding kinetics. *Med Chem Commun* 2015; 6: 1954–1958.
- Rømer J, Pyke C, Lund LR, Eriksen J, Kristensen P, Rønne E, Høyer-Hansen G, Danø K, Brünner N. Expression of uPA and its receptor by both neoplastic and stromal cells during xenograft invasion. *Int J Cancer* 1994; 57: 553–560.
- Reiter LS, Kruihof EKO, Cajot J-F, Sordat B. The role of the urokinase receptor in extracellular matrix degradation by the HT29 human colon carcinoma cells. *Int J Cancer* 1993; 53: 444–450.
- Boonstra MC, van Driel PBAA, van Willigen DM, Stammes MA, Prevoo HAJM, Tummers QRJG, Mazar AP, Beekman FJ, Kuppen PJK, van de Velde CJH, Clemens WGM, Frangioni JV, van Leeuwen FWB, Sier CFM, Vahrmeijer AL. uPAR-targeted multimodal tracer for pre- and postoperative imaging in cancer surgery. *Oncotarget* 2015; 6: 14260–14273.

35. LeBeau AM, Sevillano N, Markham K, Winter MB, Murphy ST, Hostetter DR, West J, Lowman H, Craik CS, VanBrocklin HF. Imaging active urokinase plasminogen activator in prostate cancer. *Cancer Res* 2015; 75: 1225–1235.
36. Hsiao J-K, Law B, Weissleder R, Tung C-H. *In-vivo* imaging of tumor associated urokinase-type plasminogen activator activity. *J Biomed Opt* 2006; 11 034013: 1–5.
37. Seki T, Miyasu T, Noguchi T, Hamasaki A, Sasaki R, Ozawa Y, Okukita K, Declerck PJ, Ariga T. Reciprocal regulation of tissue-type and urokinase-type plasminogen activators in the differentiation of murine preadipocyte line 3 T3-L1 and the hormonal regulation of fibrinolytic factors in the mature adipocytes. *J Cell Physiol* 2001; 189: 72–78.
38. Canello R, Rouault C, Guilhem G, Bedel JF, Poitou C, Di Blasio AM, Basdevant A, Tjorndman J, Clément K. Urokinase plasminogen activator receptor in adipose tissue macrophages of morbidly obese subjects. *Obes Facts* 2011; 4: 17–25.

SUPPORTING INFORMATION

Additional supporting information can be found in the online version of this article at the publisher's website.